# RadVIEW: Robust radar detection and characterization in high-noise regimes

Karyn Doke, Shamik Sarkar, Blessing Okoro, Danijela Cabric, Mariya Zheleva

Abstract—Accurate and objective mutual awareness between coexisting technologies is the root of trust for future spectrum sharing. Despite this, our ability for unsupervised detection of narrow-band and short-lived signals in spectrum traces is limited. This poses practical challenges in sharing spectrum with entities such as naval or weather radars, whose transmissions are inherently short-lived and often narrow-band. Ultimately, this creates a reluctance within licensed spectrum users to share their resources. Thus, the detection of short-lived and narrow-band emitters, especially in high noise scenarios, will ensure the practical applicability of dynamic spectrum sharing.

To this end, we develop RadVIEW, a lightweight and fully-unsupervised wavelet-based spectrum characterization method for detection of narrow-band and short-lived transmitters in high-noise regimes. We demonstrate RadVIEW's performance and applicability on realistically emulated naval radar traces across a wide range of signal-to-noise regimes. We show near-ideal characterization performance in comparison with counterparts from the literature. We demonstrate RadVIEW's applicability to CBRS systems and beyond as it can reduce the required Environmental Sensing Capabilities protection zones by a factor of three and detect the presence of incumbent radars in less than 0.05 seconds.

## I. Introduction

Sharing spectrum across different radio technologies has become the only feasible way forward in ensuring the necessary growth in broadband availability, while continuing to support public and defense applications. Many of the envisioned sharing scenarios will need to ensure coexistence of narrowband and short lived technologies such as navy [1], or weather radar [2], with broadband technologies such as LTE and WiFi [3], which creates unique challenges in mutual awareness and interference avoidance. To gain perspective, consider a non-chirping naval radar type 1 [4], whose bandwidth is 1MHz and its pulse duration is between 0.5 and  $2.5\mu s$ . Compared to broadband Internet signals such as WiFi or LTE, whose packet duration is in the order of several miliseconds, and bandwidth spans tens to hundreds of MHz [3], radar signals incur negligible spectrum activity. Yet, their prompt detection and protection from secondary spectrum users is essential in support of coexistence.

Limited ability to detect narrow short-lived signals has created reluctance among defense and scientific users to share their spectrum [5]. Where successful sharing policies have been established, the imposed protection measures often result in prohibitive losses in spatial spectrum reuse. A prominent example is that of Environmental Sensing Capabilities (ESC) based spectrum coexistence in the Citizen Broadband Radio Services (CBRS). In CBRS, a Spectrum Access System (SAS) allows secondary access of LTE-like technologies in

the 3.5GHz range, which is traditionally used by naval radars along coastal lines. ESC supports sensing-based coexistence, whereby coastal sensors detect the presence of radars and halt LTE transmissions. To ensure high-accuracy radar detection, however, ESCs have to be protected from interference, and thus, are enclosed by protection (whisper) zones. A recent study [5] found that nearly 40% of the US population, and 100% in some of the largest states, fall within exclusion zones. This makes ESC-based CBRS inaccessible to many consumers, and results in provider reluctance to invest in the technology. Thus, high-sensitivity detection of narrow-band and short lived transmitters is essential for next generation shared spectrum access, as it has the potential to minimize exclusion zones and improve the practical applicability of ESCbased radar detection and coexistence in CBRS and beyond. Additionally, depending on the radar type, the opportunity for secondary access will vary. For example, non-chirping navy radars operate in a 1MHz band, whereas chirping ones span a wider band of up to 20MHz. Thus, how much bandwidth is available for a secondary user will depend on the radar type they have to share with. Furthermore, radars' temporal activity varies too from type to type, thus frequency reuse over time is also possible. However, to enable efficient timefrequency sharing we must support detailed and unsupervised characterization of radar activity over time and frequency.

Radar detection has been studied in prior work both in the context of CBRS [6; 7] as well as weather radar [2]. CBRS radar detection so far [6; 7] has targeted radar detection as a binary: present/absent, however, detailed characterization of time-frequency activity has not been pursued. Furthermore, these prior works are either deep-learning based [6; 7] or rely on apriori-known cyclostationary properties of the radar [2] and thus, require supervision, while our goal is to perform unsupervised radar characterization. Finally, prior methods find challenging the detection of radar signals in low SNR regimes, which is of particular focus in our work. Finally, there are several general methods [8; 9], which tackle unsupervised transmitter characterization, however, as we demonstrate in our evaluation, these methods fall short with narrow-band and short lived signals.

To address these challenges we design RadVIEW, a lightweight unsupervised radar detection algorithm, which is highly-sensitive in low-SNR regimes. RadVIEW employs wavelet-based signal processing to denoise the temporal and frequency activity of a radar and accurately discern its time-frequency occupancy in high-noise scenarios. We demonstrate RadVIEW's performance in detecting realistic radar activity

on traces provided by NIST [4] across two radar types and six SNR levels. We show near-ideal detection accuracy even at 10dBm SNR, which as demonstrated in our evaluation, can result in a three-fold reduction of the size of the CBRS whisper zones. Finally, we demonstrate negligible characterization runtime of under 0.05 seconds, which makes RadVIEW applicable within the current CBRS timeliness requirements which require secondary users to vacate the spectrum within 300s of the detection of a radar [10].

This paper makes the following contributions:

- Novelty: We develop RadVIEW, the first fully unsupervised algorithm for detection of shortlived and narrowband signals akin radar emissions. RadVIEW is highly-sensitive and near-ideal transmitter characterization even in low-SNR regimes.
- Applicability: We demonstrate that RadVIEW is highly applicable to practical coexistence scenarios in highnoise regimes, such as those in the CBRS bands. We show that RadVIEW can reduce the currently imposed CBRS whisper zones by a factor of three while ensuring characterization time well within the SAS requirements.
- Generalizability: Because RadVIEW is unsupervised, it has a wide applicability to characterize shortlived transmissions beyond radar.

# II. RELATED WORK

Radar signal detection. As mentioned before, traditional radar signal processing relies heavily on matched filtering. This idea has been used in [11] in the context of radar detection in CBRS. However, this work uses a simplifying assumption that knowledge about the radar pulse characteristics is known at the sensor. In practice, for radar detection using a sensor, matched filtering cannot be applied as the sensor does not know the radar pulse parameters, radar center frequency, and bandwidth. Moreover, the approach in [11] cannot estimate the radar spectral and temporal characteristics.

Considering the more realistic scenario of the unavailability of radar signal parameters at the sensor, the work in [12] has investigated the use of machine learning for radar detection in CBRS. This approach relies on handcrafted feature extraction, e.g., higher-order statistics and peak statistics [12], and then uses a support vector machine (SVM) for classification. Accordingly, this method is incapable of estimating radar spectral and temporal parameters.

Several works have used deep learning, specifically by applying convolutional neural networks (CNN) on spectrograms, for the radar detection problem [13; 12; 7; 6]. While the approaches in [13; 14] improve the radar detection accuracy by virtue of efficient feature extraction of CNNs, the remaining works take one step further. Specifically, they have formulated the problem as an object detection problem and solved it using variants of the well-known YOLO algorithm [15]. Such an approach enables the additional capability of radar spectral occupancy estimation. However, treating a radar pulse burst as an object does not provide the capability to estimate the temporal parameters of the radar signal, e.g., pulse width,

inter-pulse interval, and number of pulses in a burst. The approach in [16] tackles this challenge by treating individual radar pulses as objects.

In contrast to these existing works, we take a different approach using unsupervised learning for radar detection. This advantageous as our method does not depend on a supervised model, which requires exhaustive training across all target realistic scenarios.

Unsupervised spectrum characterization has also been tackled in the literature. While most prior work deals with occupancy detection [17; 18; 19] — i.e. determining whether a band is occupied or idle without delving into transmitter properties — some have focused on detailed transmitter characterization [9; 8]. TxMiner [8] uses Rayleigh-Gaussian Mixture Models to characterize transmitter count and discern individual transmitters' time-frequency activity. AirVIEW [9] uses wavelet decomposition to denoise spectrum on a sweepby-sweep basis. Wile these approaches are well-suited to characterize long-standing spectrum activity, they both fall short when a transmitter generates minimal amounts of spectrum activity. Specifically, TxMiner is unable to model negligible transmitter activity and fails in the subsequent characterization. AirVIEW relies on long-standing emissions to tune its parameters, and is thus not directly applicable to shortlived transmissions. Additionally, AirVIEW trades accuracy for denoising, and can thus eliminate entire bursts of activity where emissions are narrow-band while attempting to denoise a trace. In contrast, RadVIEW addresses these issues by decomposing the max-hold of time and frequency activity to ensure high-sensitivity detection while not compromising with accuracy.

# III. BACKGROUND

A prominent example of narrow-band short-lived transmitters are radars, and thus, our primary focus in this paper is to explore RadVIEW's applicability to radars, even though the method is generic. In a typical radar operation, the radar transceiver first acts as a transmitter and emits a narrow pulse. Then, it acts as a receiver and waits for the return signal (transmitted pulses reflected by physical objects, e.g., aircraft). An important component of radar signal processing is matched filtering [20], which improves the signal-to-noise ratio of the received signals. Generally, radar transmitters do not send just one pulse but rather a set of equally spaced pulses to improve the probability of target detection. A set of pulses is often called a radar pulse burst.

In the context of CBRS, there are five different radar types that are relevant [21]. Among these five radar types, types 1 and 2 use pulse-modulated signals with the bandwidth of each pulse around 1 MHz. The other three radar types are frequency-chirping radars. Among these radar types, DoD navy ships, who are the primary users of the 3.5 GHz CBRS band, currently use only radar type 1, which is known as SPN-43 [12]. The other radar types are not currently used but can be deployed in the future. Hence, for our investigation in this paper, we will focus on radar types 1 and 2, which are very

TABLE I: Parameters of radar types 1 and 2

Radar	Pulse width	Inter-pulse	Bandwidth	Burst
type	(µs)	duration (ms)	(MHz)	length
1	0.5-2.5	0.91 - 1.11	1	15 - 40
2	13-52	0.33 - 3.33	1	5 - 20

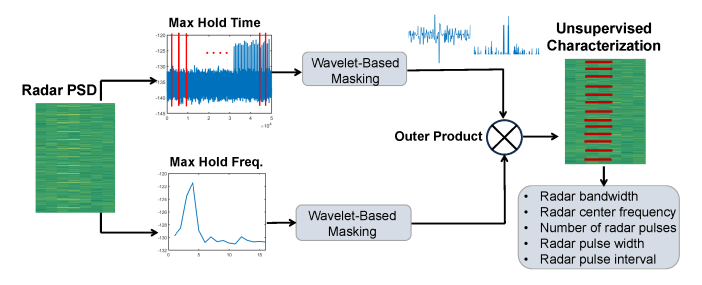


Fig. 1: RadVIEW overview.

similar. The parameters of these two radar types are tabulated in Table I. The radar pulse parameters do not change within a burst but can change across bursts.

## IV. METHODOLOGY

This section presents our methodology. Fig. 1 shows a highlevel overview of RadVIEW. RadVIEW is an unsupervised method that can detect narrow-band short-lived transmitters. Input to the model is a power spectral density (PSD) trace over frequency and time. The method characterizes temporal and frequency activity separately, as illustrated in the top (temporal) and bottom (frequency) branches of the figure. Both branches use a two-step preprocessing procedure, which focuses on denoising the scan while preserving the transmitter's time-frequency activity. The first preprocessing step finds the maxhold of time and frequency activity. The second step uses wavelet decomposition and lossy signal reconstruction to further denoise the maxholds. Denoising the entire time or frequency vectors in a single shot, however, is poised to remove radar activity, which in turn will negatively affect detection accuracy. We thus step through a maxhold in predefined chunks, whose size selection is detailed in our methodology. Wavelet-based denoising and transmitter detection are then performed in each chunk. Ultimately, each branch produces a 0-1 mask with 1s set in positions with detected transmitter activity and 0s otherwise. Having computed temporal and frequency masks we compute their outer product, which results in a full two-dimensional mask of the same size as the original data, that indicates time-frequency bins of transmitter activity. In what follows we first present our problem formulation and then provide further detail on the operation of the temporal and frequency detection.

# A. Problem Formulation

Let p(t, f)  $(t \in T, f \in F)$  be a spectrum trace of measured power spectral density (PSD) over a duration of time T and over a certain frequency band F. We define the maxhold over frequency  $P_F$  and time  $P_T$  as the maximum measured PSD in any given frequency bin (i.e. p(t, f) column) and time step (i.e. p(t, f) row), respectively. We further denote with  $W(P_F)$ 

and  $W(P_T)$  the wavelet decomposition of the frequency and time maxholds. Here W can be thought of as a function that maps  $P_F$  and  $P_T$  to a set of wavelet coefficients  $w_f$ and  $w_t$  of the same dimensionality. These wavelet coefficients can be thought of in terms of a binary tree representation with tree levels  $l \in (0, log N)$ , where N is the size of the decomposed vector (i.e. F or T). Coefficients with smaller level l are closer to the root and can facilitate aggressive signal denoising at the cost of reduced signal granularity. Conversely, coefficients closer to the leaves facilitate lesser denoising but better preserve inherent signal transitions. Let  $W^{-1}(w_t)$ (or  $W^{-1}(w_f)$ ) denote a reverse function, which reconstructs the original signal  $P_T$  (or  $P_F$ ) from the full set of wavelet coefficients  $w_t$  (or  $w_f$ ). A lossy signal reconstruction can also be obtained by only considering the wavelet coefficient  $w_t(l)$ (or  $w_f(l)$ ) at a certain level l of their binary tree representation. Such a lossy reconstruction can serve as a powerful denoiser, as demonstrated in [9]. Thus, let  $\hat{P_T^l}=W^{-1}(w_t(l))$  be a lossy reconstruction of the signal's temporal maxhold, and  $P_F^l = W^{-1}(w_f(l))$  a lossy reconstruction of the signal's frequency maxhold. To emphasize the transmitter activity while denoising even further [9], we next compute the multiscale product  $\pi^l$  of lossy signal reconstructions at neighboring scales l and l-1. E.g. the multiscale product for the temporal maxhold at scale l would be  $\pi_T^l = \hat{P}_T^l * \hat{P}_T^{l-1}$ . Finally, we denote with  $\Delta_\pi$  the absolute pairwise difference between consecutive values in  $\pi^l$ . For example,  $\Delta_{\pi^l_T}=|\pi^l_T(t)-\pi^l_T(t+1)|$  is the absolute pairwise difference between consecutive values in the multiscale product of  $P_T^l$ . As noted earlier, the selection of ltrades denoising with signal granularity. This is particularly important in the case of narrow-band short-lived transmitter detection, as too aggressive denoising might obliviate target transmitter activity from the trace. Thus, for the purposes of our methodology, we always select the level immediately above the tree leaves (i.e. l = log N - 1). This allows for sufficient denoising while preserving the transmitter's inherent time-frequency properties. Furthermore, we use the Haar Wavelet as a mother wavelet for our decomposition, as it best represents the rectangular signal transitions characteristic to transmitter activity.

#### B. RadVIEW algorithm

Algorithm 1 presents our approach. It takes as an input a matrix of PSD over time and frequencies (p(t,f)) and produces a mask  $\Omega$  of the same dimensionality, which indicates time-frequency blocks that are occupied. The algorithm first computes the time and frequency maxholds of the input data. It then performs unsupervised learning of a detection threshold  $\tau$ , which we describe later. RadVIEW then characterizes the temporal and frequency activity in turn, as detailed in Algorithm 2. The maxholds are analyzed in chunks of size c, as indicated in line 1. For each chunk, the method first computes the wavelet decomposition  $W(P_i)$  and a lossy signal reconstruction  $\hat{P}_i^l$  at levels l and l-1. It then computes the multiscale product  $\pi_i^l$  of these lossy reconstructions, and finds

## Algorithm 1 RadVIEW

```
\begin{array}{ll} \textbf{Input:} & p(t,f) \\ \textbf{Output:} & \Omega \; \{ \text{A 0-1 mask of transmitter activity} \} \\ 1: & \text{Compute} \; P_F = \max_{f \in F}(p(t,f)) \; \text{and} \; P_T = \max_{t \in T}(p(t,f)) \\ & \{ \text{Learn detection threshold} \} \\ 2: & \tau = \text{learnthr} \; (P_T) \; \{ \text{Run Alg. 3 on } P_T \} \\ & \{ \text{Temporal characterization} \} \\ 3: & \Omega_T = \text{WaveMask} \; (P_T, \; c, \; \tau) \; \{ \text{Run Alg. 2 on } P_T \} \\ & \{ \text{Frequency characterization} \} \\ 4: & \Omega_F = \text{WaveMask} \; (P_F, \; c, \; \tau) \; \{ \text{Run Alg. 2 on } P_F \} \\ 5: & \Omega = \Omega_f \otimes \Omega_T \\ \end{array}
```

# Algorithm 2 Wavelet-based masking

```
\begin{array}{ll} \textbf{Input:} & \text{A maxhold of PSD } P \text{, a chunk size } c \text{ and a threshold } \tau \\ \textbf{Output:} & \Omega \left\{ \text{A } 0\text{-1 mask of transmitter activity} \right\} \\ 1: & \textbf{for } i=1:c:T \textbf{ do} \\ 2: & \text{Compute } W(P_i), \ \hat{P}_i^l \text{ and } P_i^{\hat{l}-1} \\ 3: & \text{Compute } \pi_i^l = \hat{P}_i^l * P_i^{\hat{l}-1} \\ 4: & \text{Compute } \Delta_{\pi^l} = |\pi_i^t - \pi_i^{(t+1)}| \\ 5: & \text{Find all components } j \text{ in } \Delta_{\pi^l} \text{ that exceed } \tau \\ 6: & \text{Produce a detection mask } \Omega_{c_i} \text{ for chunk } c_i \\ 7: & \textbf{end for} \\ 8: & \text{Reconcile full detection mask } \Omega = < \Omega_{c_i} > \\ \end{array}
```

the absolute pairwise differences between adjacent values in the product. At this stage (line 4 of Algorithm 2) the algorithm produces a denoised version of the maxhold, which is ready for high-sensitivity characterization. The characterization is performed in line 5 against a previously-learned threshold  $\tau$ , resulting in a detection mask  $\Omega_{c_i}$  which indicates idle and occupied regions of chunk  $c_i$ . Once all chunks are processed, Algorithm 2 reconciles the individual  $\Omega_{c_i}$  into a single detection mask  $\Omega$  and returns this to RadVIEW.

As mentioned earlier, an important step of RadVIEW is characterizing the denoised signal representation  $\Delta_{\pi^l}$  against an adaptively learned threshold au. Our threshold selection methodology is outlined in Algorithm 3. We employ a divideand-conquer procedure that takes as an input a maxhold (time or frequency), and splits it recursively into s equal-sized slices. At each recursion level, each of the resulting slices is cast into a vector of absolute pair-wise differences (line 5), akin the one calculated in line 4 of Algorithm 2. We then calculate a candidate threshold at the i = th recursive split as one half of the difference between the maximum and minimum values of  $\Delta \pi_{P_i}$  (line 6). This results in  $s=2^i$ candidate thresholds per recursive split. We take the maximum of these thresholds (line 8, as it is most likely to represent a slice with both noise and transmitter activity. Intuitively, thresholds learned early in the recursion will be based on a decomposition of the entire signal, which as noted earlier is poised to obliviate narrow-band or short-lived activity. The resulting thresholds will thus be small, as no pronounced peaks indicating transmitter activity will be present. As we get deeper into the recursion, we will begin preserving inherent signal features in the decompsed/denoised signal, and the corresponding thresholds will better represent the range of the measured signal. Eventually, we reach a level of recursive splitting where the threshold no longer changes, which indicates that our

# Algorithm 3 Adaptive threshold selection

```
Input: Temporal maxhold P_T, number of recursive splits S
Output: Transmitter detection threshold \tau
1: for i = 1 : S do
2:
        for j = 1 : s do
3:
            Compute wavelet decomposition W(P_i)
4:
            Compute multiscale product of lossy reconstructions \pi_{P_i}
            Compute \Delta \pi_{P_j} = |\pi_{P_j}^t - \pi_{P_j}^{(t+1)}|
\max(\Delta \pi_{P_j}) - \min(\Delta \pi_{P_j})
5:
6.
7:
8:
        Find \tau_i = max_s(\tau_i)
9.
        if \tau_i - \tau_{i-1} \leq \epsilon then
10:
        end if
11:
12: end for
```

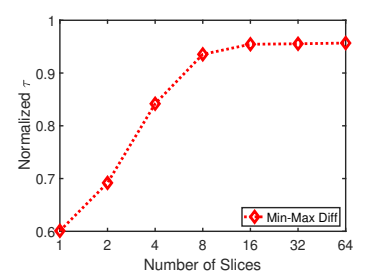


Fig. 2: Adaptive normalized threshold  $\tau$ .

adaptive learning has converged to the optimal threshold. An example of threshold learning for a single temporal maxhold is presented in Figure 2, where the x-axis presents the number of equisized slices s, while the y-axis presents a normalized threshold  $\tau$ . The threshold plateaus at 8 slices, indicating that the optimal threshold can be found with three recursive splits.

Another important RadVIEW parameter is the step size c with which we step through the temporal and frequency maxholds as we analyze them (line 1 in Algorithm 2). A step too large will preclude transmitter detection. Thus, we want to select a step that closely encompasses a temporal or frequency burst. For a target radar with known parameters, the size of each burst can empirically inform c, so it does not need to be estimated. We demonstrate the importance of selecting a proper c in Figure 3, which presents the accuracy of duration detection for single pulse with increasing chunk size c for radar type 1 (left) and type 2 (right). For type 1 radar we observe that after c=32 the accuracy for SNR 10 and 12 drops to 0. SNR 14 drops to 0 after S=64. Likewise for radar type 2, SNR 10, 12, and 14 drop to 0 after S=128. Intuitively, since radar type 1 has shorter pulse duration (Table I), it will require a smaller step to be detected. Radar type 2, in turn, uses longer pulses and can thus tolerate larger step sizes. THe sensitivity to the step size also depends on SNR, whereby pulses can be detected even within larger steps where the SNR is high. For the purposes of our evaluation we select c=32 as it can accurately detect both radar types across all SNR values.

# V. EVALUATION

In this section, we first describe our experimental setup and then present our evaluation results.

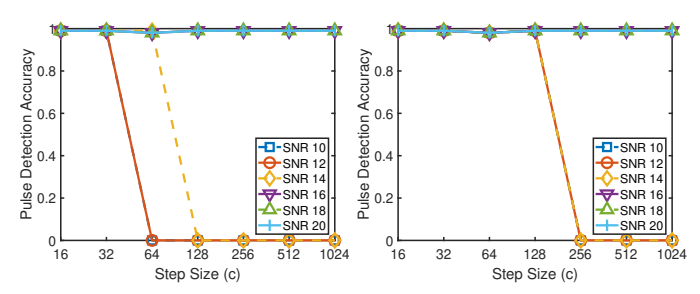


Fig. 3: Pulse detection accuracy with increasing step size for type 1 (left) and type 2 (right).

# A. Experimental Setup

Dataset. We employ an RF dataset of incumbent radar systems in 3.5 GHz CBRS band [4] to test and evaluate RadVIEW. The dataset consists of synthetically generated radar waveforms in an IO complex format. The dataset is generated with added white Gaussian noise across five radar types {P0N#1, P0N#2, Q3N#1, Q3N#2, Q3N#3} and across SNR ranges {10, 12, 14, 16, 18, 20. The first two radar types (types 1 and 2) are pulsemodulated signals with the bandwidth of each pulse around 1 MHz. The other three radar types (types 3, 4, and 5) are frequency-chirping radars. For the purpose of this paper, we focus on pulse-modulated signals. The dataset is accompanied with some meta data information about the waveforms. The pulse width  $(\Delta T)$ , pulses per second (N), pulses per burst (K) ranges for radar types 1 and 2 are outlined in Table I. The radar center frequency  $(f_c)$  is a random frequency shift for radar types 1 and 2 with a varying start time  $(t_0)$ . The bandwidth ( $\Delta F$ ) of the signal is 1 MHz, the sampling rate ( $f_s$ ) is 10 MHz and the waveform duration (T) is 0.08 seconds. In all experiments, we use a subset of traces from the dataset. We evaluate RadVIEW using traces for radar type 1 (P0N#1) and type 2 (P0N#2) across the following SNR values: 10, 12, 14, 16, 18, 20. For each radar type and SNR value, we select 20 traces.

**Groundtruth.** From this meta data, we can derive the groundtruth necessary to evaluate RadVIEW. we introduce the following metrics to convert pulse width  $(\Delta T)$ , bandwidth  $(\Delta F)$  and inter-arrival time  $(\tau)$  to scan rows. We convert pulse width to scan rows  $(\Delta T')$  by the following:

$$\Delta T' = \lceil \frac{\Delta T}{\Delta t} \rceil \tag{1}$$

where  $\Delta t$  is row duration calculated by  $\frac{FFT}{f_s}$ .

Bandwidth  $(\Delta F)$  can be converted to scan rows  $(\Delta F')$  by the following:

$$\Delta F' = \lceil \frac{\Delta F}{\Delta f} \rceil \tag{2}$$

where  $\Delta f$  is the frequency resolution given by  $\frac{f_s}{FFT}$ . We calculate the radar inter-arrival time by:

$$\tau = \frac{1}{N} \tag{3}$$

where N is the pulses per second. From this, we can convert the inter-arrival time to scan rows using:

$$\tau' = \lceil \frac{\tau}{\Delta t} \rceil \tag{4}$$

where  $\Delta t$  is the row duration as derived above.

**Baselines.** We compare against two counterparts from the literature: Txminer [8] and AirVIEW [9]. We run both counterparts on the same input p(t,f) we supply to RadVIEW. Due to their limitations outlined in Section II, both counterparts fail to characterize the radar signals. We demonstrate this through a qualitative analysis presented in Section V-C.

**Evaluation metrics.** We evaluate RadVIEW's accuracy in detecting radar properties including bandwidth, pulse duration, and pulse inter-arrival time. To this end, we utilize the following accuracy metrics: bandwidth accuracy  $A_{\Delta F}$ , pulse duration accuracy  $A_{\Delta T}$  and pulse inter-arrival time accuracy  $A_{\Delta T}$ .

Bandwidth accuracy it calculated by:

$$A_{\Delta F} = \frac{1}{|\mathcal{B}|} \sum_{B: \in \mathcal{B}} \frac{|B_i \cap O_j|}{|B_i|} \tag{5}$$

where  $\mathcal{O}=\{O_j\}$  is set of frequency bins detected as occupied and  $\mathcal{B}=\{B_i\}$  is the set of occupied bins per the groundtruth.  $|B_i\cap O_j|$  denotes the intersection of  $B_i$  and  $O_j$ .

Pulse duration accuracy is calculated by:

$$A_{\Delta T} = \frac{1}{|\mathcal{K}|} \sum \frac{|D_i|}{|\Delta T|} \tag{6}$$

where  $D_i$  is the detected pulse duration in scan sweeps,  $\mathcal{K}$  is the total number of pulses in the trace, and  $\Delta T$  is the pulse duration in scan sweeps per the groundtruth.

Finally, pulse inter-arrival accuracy is calculated by:

$$A_{\tau} = \frac{1}{|\mathcal{K} - 1|} \sum \frac{|I_j|}{|\tau|} \tag{7}$$

where  $I_j$  is the pulse inter-arrival duration in scan sweeps, K is the total number of pulses in the trace, and  $\tau$  is the pulse inter-arrival duration in scan sweeps per ground truth.

**Implementation.** We implement RadVIEW as a single-thread Java program where all experiments are executed on commodity desktop.

# B. RadVIEW performance

We now evaluate RadVIEW 's performance. We explore accuracy of radar characterization considering two important components of the algorithm: the chunk size c at which we step through the time/frequency maxhold and the level of recursive splits S used to learn the detection threshold  $\tau$ . Figure 4 presents our results for bandwidth (left), duration (middle) and pulse interarrival time (right) detection with increasing SNR. Red represents radar type 1, whereas blue is radar type 2. The different line textures represent three levels of slicing (1, 2 and 3), which result in 2, 4 and 8 slices respectively. As noted in our methodology, splitting in 8 or more slices converges to the optimal threshold for our data. We see this reflected in the performance reported performance, whereby RadVIEW achieves

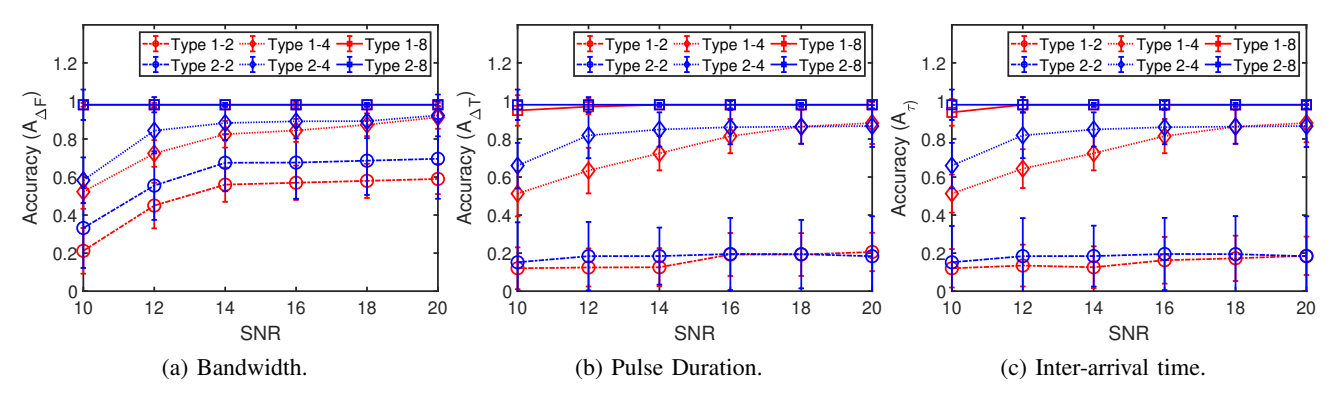


Fig. 4: RadVIEW accuracy over SNR with increasing recursion depth for the adaptive threshold learning.

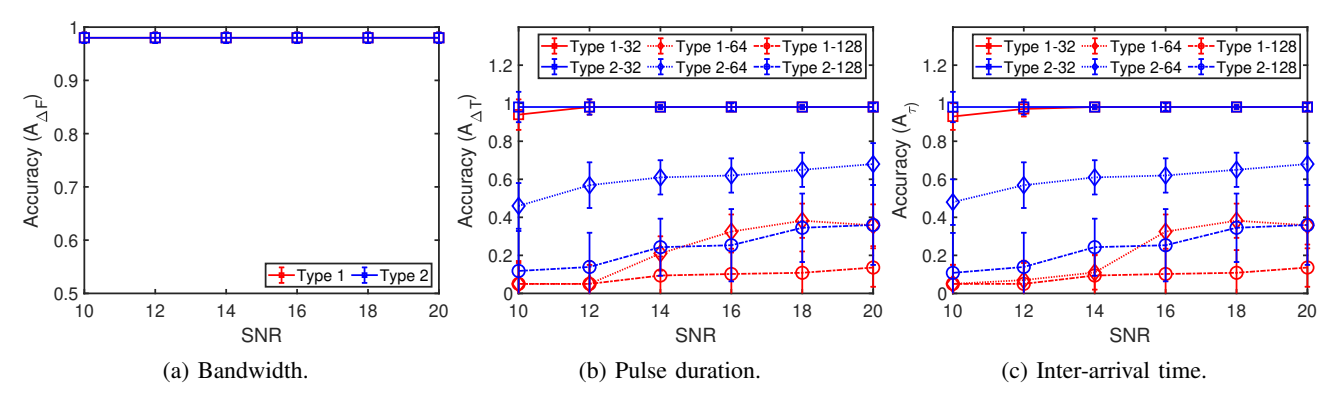


Fig. 5: RadVIEW accuracy over SNR with increasing chunk size c.

near-perfect accuracy with 8 slices and deteriorates due to the suboptimal thresholds learned with fewer slices. Additionally, we explore RadVIEW's performance with increasing chunk sizes  $c \in (32,64,128)$  in Figure 5. We note that the chunk size has no effect on our frequency detection (left), as the traces we use are inherently narrowband (only 16 bins wide). The two temporal properties: pulse duration and interarrival time, are both sensitive to the chunk size with both deteriorating as c increases to 64 and beyond.

## C. Qualitative comparison with baselines

Next we present a qualitative analysis comparing RadVIEW with two counterparts of literature, AirVIEW and TXminer. We compare the performance of these models using two type 2 radar traces representing a low (10 dB) and a high (20 dB) SNR. We input each radar trace to each of the three models and generate a binary matrix spectrogram. AirVIEW takes as input the full trace and uses a parameter estimation to find the optimal parameters. Table II presents our results. The first column represents the output from RadVIEW, the second column the output from AirVIEW and the last column the output from TXminer. The spectrograms representing the output from RadVIEW and from AirVIEW are enlarged for clarity so that the detections can be seen. Each row contains the respective radar trace with the corresponding SNR. Across all SNRs, RadVIEW is able to accurately detect the radar burst. In all cases, AirVIEW and TxMiner are unable to detect the radar activity. AirVIEW falls short in denoising narrow-band and short-lived pulses. TxMiner, in turn, is unable to adequately model the transmitter activity due to the negligible representation of transmitter values in the overall trace.

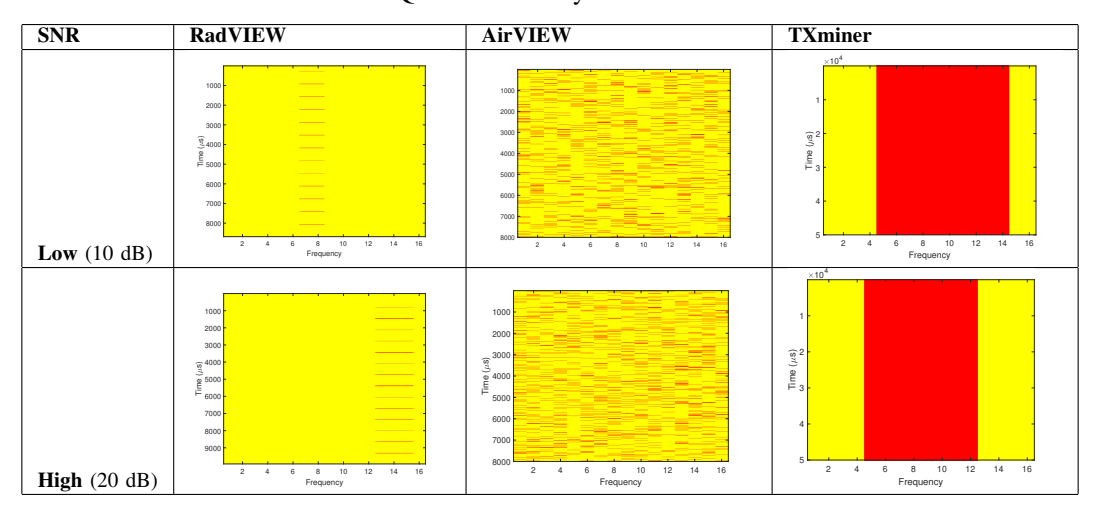
# D. Timeliness of Radar Detection

In CBRS, the detection of radar must be reported to the SAS in a timely fashion. Based on this reported information, the SAS will free up the bands in which devices may interfere with the radar signals. Radar pulses are extremely shortlived and must be detected within 60 seconds [11] to avoid interference with defense applications. As a result, we want to evaluate RadVIEW in terms of how fast we can detect radar activity. Fig. 6 presents the runtime for radar detection and characterization across increasing pulse bursts for radar type 1. For radar type 1, the range of pulse bursts is 15-40, as outlined in Table I. From the figure, we see that the runtime to detect and characterize 25 bursts is 44 ms. Additionally, we evaluate the RadVIEW in terms of how fast we can select the threshold. The runtime to select the threshold is 9 ms.

# E. Implications on CBRS Protection Zones and Ubiquity

An important implication of our work is that it can address the problem of whisper zones [22; 23] to some extent. The problem with the whisper zones of the ECSs in CBRS is that the ESCs must have interference protection from the secondary transmitters to be able to reliably detect the incumbent radar

TABLE II: Qualitative Analysis of Radar Detection



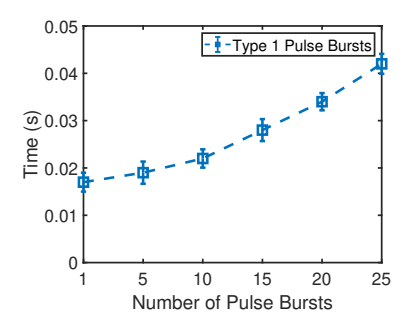


Fig. 6: Runtime (s) for radar detection and characterization across increasing pulse bursts for type 1 radar.

signals. In the context of CBRS, the secondary transmitters are the Priority Access Licensed (PAL) and Generally Authorized Access (GAL) users. As a result of this interference protection zone, secondary base stations (BS) cannot be deployed in the vicinity of the ECSs, which is known as the whisper zone. In fact, in some scenarios, the whisper zone can have a radius of about 80 km from the ESC.

The problem of whisper zones can be alleviated if the ESCs can reliably detect the radar signals even in the presence of interference from the secondary BSs, i.e., the ESC can reliably perform radar detection at lower radar signal to interference and noise ratio (SINR). Assuming that the aggregate interference at the ESCs can be modeled as AWGN [24], a lower SINR is equivalent to a lower SNR. As per the current set of CBRS rules, the ESC must be able to detect radar signals with more than 99% accuracy when the peak radar signal power is ≥ -89 dBm/MHz and the aggregate interference average power at the ESC is  $\leq$  -109 dBm/MHz [21]. In other words, the ESC must detect radar signals accurately at 20 dB radar SNR (peakto-average). If we can bring down this SNR to 10 dB without compromising the radar detection accuracy, then we can bring the secondary transmitters closer to the ESC. I.e., for radar signal power of -89 dBm/MHz at the ESC, a 10 dB reduction in radar SNR implies the aggregate interference at the ESC can be as high as -99 dBm/MHz. Using a simple radio wave propagation path loss model [25], we show below that for a single interfering secondary BS if the ESC can detect radar signals at 10 dB radar SNR, then the whisper zone radius can be reduced by three times.

For the case of 20 dB radar SNR at the ESC, we can write

$$P_R^{20}(dBm) = P_0(dBm) - 10\eta log_{10}(\frac{d_{20}}{d_0})$$

where  $P_R^{20}$  dBm is the received power at the ESC from a BS at the end of the whisper zone,  $d_{20}$  m is the radius of the whisper zone,  $\eta$  is the radio wave propagation path loss exponent, and  $P_0$  (dBm) is the received power at a reference distance of  $d_0$  m. Similarly, in the case of 10 dB radar SNR at the ESC, we can write

$$P_R^{10}({\rm dBm}) = P_0({\rm dBm}) - 10\eta log_{10}(\frac{d_{10}}{d_0})$$

where  $P_R^{10}$  dBm is the received power at the ESC from a BS at the end of the whisper zone, and  $d_{10}$  m is the radius of the whisper zone. If the radar signal power is fixed, then a drop of 10 dB radar SNR implies,  $P_R^{10} - P_R^{20} = 10$ . Hence, using the above two equations we can write,

$$10 = P_R^{10} - P_R^{20} = 10\eta log_{10}(\frac{d_{20}}{d_0}) - 10\eta log_{10}(\frac{d_{10}}{d_0})$$

This can be simplified as:

$$d_{10} = \frac{d_{20}}{10^{1/\eta}}$$

For  $\eta=2$ ,  $d_{10}=d_{20}/3.16$ . It is evident from the above example that the reduction in whisper zone radius will be lower than the presented example if the number of interfering BSs is more than one.

Note that although we presented the above discussion for fixed radar signal power and increasing interference power, the dataset that we use in our evaluations has fixed noise power and reduced radar signal power. However, our method would perform equally well if the radar signal power was fixed and the noise power was increased as our method is an unsupervised learning method.

# VI. DISCUSSION AND CONCLUSION

We develop RadVIEW, an unsupervised algorithm for highsensitivity detection of narrow-band fleeting transmitters. We demonstrate RadVIEW's ability to detect realistic navy radar signals akin to these operating in the 3.5GHz CBRS bands. With its high sensitivity RadVIEW can reduce CBRS's Environmental Sensing Capabilities whisper zones by a factor of three while amply meeting the standard's timeliness requirements for secondary users to detect incumbents and vacate the spectrum. While RadVIEW is an important first step in detection of narrow-band fleeting transmitters with high noise, we are still limited in discerning such fleeting transmitters when they co-occur with broadband longstanding interferers. Our future work will focus on this problem, as it is essential for the complete elimination of whisper zones and can provide trustworthy and actionable insights for spectrum enforcement in primary-secondary coexistence scenarios.

#### REFERENCES

- [1] "Federal communications commision, 3.5 ghz band overview,"

  Downloaded from https://www.fcc.gov/wireless/bureau-divisions/
  mobility-division/35-ghz-band/35-ghz-band-overview.
- [2] Z. Khan, J. J. Lehtomaki, R. Vuohtoniemi, E. Hossain, and L. A. DaSilva, "On opportunistic spectrum access in radar bands: Lessons learned from measurement of weather radar signals," *IEEE Wireless Communications*, vol. 23, no. 3, pp. 40–48, 2016.
- [3] "Ieee standard for information technology-telecommunications and information exchange between systems local and metropolitan area networks-specific requirements part 11: Wireless lan medium access control (mac) and physical layer (phy) specifications amendment 1: Enhancements for high-efficiency wlan," *IEEE Std 802.11ax-2021 (Amend*ment to IEEE Std 802.11-2020), pp. 1–767, 2021.
- [4] R. Caromi, M. Souryal, and T. A. Hall, "RF Dataset of incumbent radar systems in the 3.5 ghz cbrs band, national institute of standards and technology," Downloaded from https://data.nist.gov/od/id/mds2-2116, Dec. 2019.
- [5] M. Zheleva, C. R. Anderson, M. Aksoy, J. T. Johnson, H. Affinnih, and C. G. DePree, "Radio dynamic zones: Motivations, challenges, and opportunities to catalyze spectrum coexistence," *IEEE Communications Magazine*, 2023.
- [6] N. Soltani, V. Chaudhary, D. Roy, and K. Chowdhury, "Finding waldo in the cbrs band: Signal detection and localization in the 3.5 ghz spectrum," in GLOBECOM 2022-2022 IEEE Global Communications Conference. IEEE, 2022, pp. 4570–4575.
- [7] S. Sarkar, M. Buddhikot, A. Baset, and S. K. Kasera, "Deepradar: A deep-learning-based environmental sensing capability sensor design for cbrs," in *Proceedings of the 27th Annual International Conference on Mobile Computing and Networking*, 2021, pp. 56–68.
- [8] M. Zheleva, R. Chandra, A. Chowdhery, A. Kapoor, and P. Garnett, "Txminer: Identifying transmitters in real-world spectrum measurements," in 2015 IEEE International Symposium on Dynamic Spectrum Access Networks (DySPAN). IEEE, 2015, pp. 94–105.

- [9] M. Zheleva, P. Bogdanov, T. Larock, and P. Schmitt, "Airview: Unsupervised transmitter detection for next generation spectrum sensing," in *IEEE INFOCOM 2018-IEEE Conference on Computer Communications*. IEEE, 2018, pp. 1673–1681.
- [10] A. Sahoo, N. El Ouni, and V. Shenoy, "A study of timing constraints and sas overload of sas-cbsd protocol in the cbrs band," in 2019 IEEE Globecom Workshops (GC Wkshps). IEEE, 2019, pp. 1–6.
- [11] R. Caromi, M. Souryal, and W.-B. Yang, "Detection of incumbent radar in the 3.5 ghz cbrs band," in 2018 IEEE Global Conference on Signal and Information Processing (GlobalSIP). IEEE, 2018, pp. 241–245.
- [12] R. Caromi and M. Souryal, "Detection of incumbent radar in the 3.5 ghz cbrs band using support vector machines," in 2019 Sensor Signal Processing for Defence Conference (SSPD). IEEE, 2019, pp. 1–5.
- [13] A. Selim et al., "Spectrum monitoring for radar bands using deep convolutional neural networks," in GLOBECOM 2017-2017 IEEE Global Communications Conference. IEEE, 2017, pp. 1–6.
   [14] W. M. Lees et al., "Deep Learning Classification of 3.5 GHz Band Spec-
- [14] W. M. Lees et al., "Deep Learning Classification of 3.5 GHz Band Spectrograms with Applications to Spectrum Sensing," *IEEE Transactions on Cognitive Communications and Networking*, 2019.
- [15] J. Redmon, S. Divvala, R. Girshick, and A. Farhadi, "You only look once: Unified, real-time object detection," in *Proceedings of the IEEE* conference on computer vision and pattern recognition, 2016, pp. 779– 788
- [16] S. Sarkar, D. Guo, and D. Cabric, "Radyololet: Radar detection and parameter estimation using yolo and wavelet," arXiv preprint arXiv:2309.12094, 2023.
- [17] T. Yucek and H. Arslan, "A survey of spectrum sensing algorithms for cognitive radio applications," *IEEE Communications Surveys Tutorials*, vol. 11, no. 1, pp. 116–130, Jan 2009.
- [18] S. D. Jones, E. Jung, X. Liu, N. Merheb, and I.-J. Wang, "Characterization of Spectrum Activities in the U.S. Public Safety Band for Opportunistic Spectrum Access," in Proceedings of the 2007 2Nd IEEE International Symposium on New Frontiers in Dynamic Spectrum Access Networks. Washington, DC, USA: IEEE Computer Society, 2007, pp. 137–146. [Online]. Available: http://dx.doi.org/10.1109/DYSPAN.2007.26
- [19] Z. Tian and G. Giannakis, "A wavelet approach to wideband spectrum sensing for cognitive radios," in *CROWNCOM*, Mykonos Island, Greece, June 2006.
- [20] M. A. Richards, J. Scheer, W. A. Holm, and W. L. Melvin, *Principles of modern radar*. Citeseer, 2010, vol. 1.
- [21] F. H. Sanders, J. E. Carroll, G. A. Sanders, R. L. Sole, J. S. Devereux, and E. F. Drocella, "Procedures for laboratory testing of environmental sensing capability sensor devices," *Techincal Memorandum TM*, pp. 18– 527, 2017.
- [22] A. W. Clegg *et al.*, "Radar sharing in the us 3 ghz band," in 2022 IEEE Radar Conference. IEEE, 2022, pp. 1–5.
- [23] "Potential Metrics for Assessing the Impact of ESC Sensors and Networks on CBRS Deployments," https://winnf.memberclicks.net/assets/work\\_products/Reports/WINNF-TR-1015-V1.0.0\%20ESC\%20Sensor\%20Impact\%20Technical\%20Report.pdf.
- [24] F. H. Sanders, J. E. Carroll, G. Sanders, R. L. Sole, R. J. Achatz, and L. S. Cohen, EMC measurements for spectrum sharing between LTE signals and radar receivers. Institute for Telecommunication Sciences, National Telecommunications & Information Administration, US Department of Commerce, 2014.
- [25] T. S. Rappaport et al., Wireless Communications: Principles and Practice. prentice hall PTR New Jersey, 1996, vol. 2.